



EUROPEAN
COMMISSION

Community Research



FP7-Fission-2013
Combination of Collaborative project (CP) and Coordination and Support Actions (CSA)

Grant agreement no: 604862
Start date: 01/11/2013 Duration: 48 Months

D-2.1.2

***Development of interatomic potential for bcc
FeCrNi(Si/P) and its validation***

MatISSE – Contract Number: 604862

Document title	Development of interatomic potential for bcc FeCrNi(Si/P) and its validation
Author(s)	Giovanni Bonny (SCK•CEN), Alexander Bakaev (SCK•CEN), Matthias Posselt (HZDR), Evgeny Zhurkin (Polytechnic University of St. Petersburg)
Number of pages	18
Document type	Report
Work Package	2
Document number	D2.12
Issued by	SCK•CEN
Date of completion	23/02/2016
Dissemination level	Public

Summary

We have developed a ternary potential for the ferritic FeNiCr system and applied it to study the formation of NiCr clusters near dislocation loops by means of MMC simulations. The potential was fitted to point defect properties and the Ni solubility limit in bcc Fe.

The potential has shown to reproduce the most stable interstitial configurations predicted by DFT. In addition, the potential can reproduce DFT logic with respect to the binding energy of small substitutional defect clusters.

In defect free alloys the MMC simulations have shown that the presence of Cr slightly increases the Ni solubility, while the presence of Ni does not affect the Cr solubility.

From our MMC simulations we found that the presence of dislocation loops increases the Cr solubility limit by about 100 K for low concentrations of Ni, i.e., in Fe-10Cr-0.25Ni and Fe-10Cr-0.50Ni alloys. In Fe-10Cr-Ni alloys both $\frac{1}{2}\langle 111 \rangle$ and $\langle 100 \rangle$ loops contribute to the increase of Ni solubility, starting from concentrations of Ni equal to 1% and 0.5%, respectively. Thus, Cr plays a stabilizing role for the Ni clusters while the addition of Ni decreases the segregation of Cr, leading to depletion of Cr above 1% of Ni. In FeNi alloys the segregation of Ni at dislocation loops is stronger than in Fe-10Cr-Ni up to 1% for $\langle 100 \rangle$ loops and for all concentrations of Ni studied for $\frac{1}{2}\langle 111 \rangle$ loops.

No synergetic effects were found for Ni and Cr with respect to segregation, except for the case of $\frac{1}{2}\langle 111 \rangle$ dislocation loops at 300 K where the total segregation in Fe-10Cr-Ni is much lower than the cumulative segregation in Fe-10Cr and relevant FeNi alloys.

1 Introduction

High-chromium ferritic-martensitic steels (~9-12 at% Cr) are the materials of choice for high temperature applications in aggressive environments (e.g. corrosion and/or irradiation). As a consequence, they are the commonly proposed structural materials for advanced nuclear reactors [1-3]. This choice is supported by their superior thermal, corrosion and radiation resistance compared to austenitic steels [4].

Irradiation campaigns on FeCr alloys – model alloy for F-M steels – have shown that the hardening due to neutron irradiation can be attributed to a microstructure containing dislocation loops, α' precipitates and NiSiPCr clusters [5-7]. While a lot of research has focused on α' precipitation [8-14] and dislocation loops in FeCr alloys [15-17], not so much is known about NiSiPCr clusters. The latter are observed under both ion and neutron irradiation using atom probe tomography (APT) [7, 18-20]. They are suggested to be irradiation induced and might be associated to small invisible dislocation loops [18, 19]. In support of the experiments, atomistic simulations are desirable.

As the next step from FeCr model alloys and a first step towards the chemical complexity of steels, we develop a ternary FeNiCr potential. The ultimate goal is to use this potential to assess the effect of Ni on the hardening due to NiCr clusters and NiCr enriched dislocation loops.

In this work we develop a bcc FeNiCr potential and apply it to investigate the thermal stability of NiCr clusters in bcc Fe with and without defect clusters. As defect clusters we consider $\frac{1}{2}\langle 111 \rangle$ and $\langle 100 \rangle$ loops.

2 Methodology

2.1 Interatomic Potential

In this work we use embedded atom method (EAM)-like [21] potentials as a compromise between performance and physical accuracy. The latter formalism has been widely used to fit potentials for metals [22-25] and their alloys [26-39].

In the literature many EAM-based potentials are available to describe the FeNiCr system [26, 27, 36, 38]. However, they were all fitted to describe the fcc phase and no potential is available to describe the bcc FeNiCr phase. Therefore such a potential is fitted here, whilst trying to take advantage of the current state-of-the-art.

For the FeCr system, five EAM-like potentials that reproduce the change of sign in the mixing enthalpy as predicted by DFT [40-46] are available in the literature. Two potentials were fitted in the concentration dependent model (CDM) [32] and three in the two-band model (2BM) [33]. The original CDM potential was fitted by Caro et al [32] with an emphasis on the reproduction of the mixing enthalpy. Later del Rio et al [37] modified the latter to account for point defect properties. The original 2BM potential was fitted by Olsson et al [33] as a compromise between reproduction of the mixing enthalpy and point defect properties. Later Bonny et al [35] improved the potential with respect to thermodynamics and point defect properties. The latest 2BM potential was developed by Eich et al [39] with an emphasis on thermodynamics. In this work we choose to use the potential by Bonny et al [35] that has been widely used and tested [47-52]. In addition, all results obtained in this work are consistent with our previous work.

For the FeNi system many EAM-like potentials are available [28-31]. However, only the one developed by Bonny et al [34] was fitted as a compromise between reproduction of the lattice stabilities of several intermetallic compounds and point defect properties in bcc FeNi alloys. As a result, one of its main shortcomings is a failure to reproduce vacancy-Ni binding at both first and second nearest neighbor distance [34] and an overestimation of the Ni solubility limit in bcc Fe by about a factor five [53]. In order to improve on these two shortcomings we fitted a new FeNi in this work.

For pure Fe we chose the EAM potential developed by Mendeleev *et al.* [24] ('potential 2'). This potential is compatible with the one used for FeCr and has been widely used and tested with respect to radiation damage studies [54] and dislocation properties [55].

For pure Ni we used one of the most recent EAM potentials developed by Mishin et al. [25]. Thus, in this work we fit the FeNi and NiCr cross pair potentials. Additional s-density functions for NiFe and NiCr, as well as an s-embedding function for Ni are physically unnecessary. Therefore they are set to zero.

Both FeNi and NiCr cross potentials were fitted with low priority to Rose's equation of state [56] and the elastic constants of the $L1_3$ FeNi₃ [57, 58, 31] and Ni₂Cr [59, 60] intermetallic compounds, respectively. Although the latter properties are not of interest for this work, they guarantee a reasonable physical shape of the cross pair potentials.

The FeNi cross pair potential was fitted as a compromise between the DFT calculated vacancy-Ni binding energy [61], Calphad calculated Ni solubility limit [62], DFT calculated Ni-vacancy exchange migration barrier [63] and DFT calculated mixed FeNi dumbbell binding energy [61] in bcc Fe. The NiCr cross pair potential was fitted to reproduce the DFT calculated binding energy of NiCr pairs [64] and mixed NiCr dumbbell in bcc Fe [64]. The optimized parameterization of both cross pair potentials is presented in Annex I.

2.2 Monte Carlo Simulations

In this work the phase boundaries were estimated by means of Metropolis Monte Carlo (MMC) sampling [65] within the isobaric semi-grand canonical ensemble ($N, P, T, \Delta\mu$) for defect free binary alloys and the isobaric grand canonical ensemble (N, P, T) for ternary alloys and binary alloys containing defects. Both MMC methods include three types of trials of which two are common to both methods: (i) a random displacement of all atoms from their current positions (by this trial lattice relaxation and vibrational entropy are accounted for); (ii) the overall volume change of the simulation box (this trial allows the desired pressure to be maintained, even if a structural transition were to occur). In the semi-grand canonical ensemble the third trial consists of the change of species of a randomly picked atom (by this trial the equilibrium composition is sampled), while in the grand canonical ensemble the latter consists of the random exchange of two atoms of different species (by this trial the equilibrium configurations are sampled). The decision on the acceptance of the new configuration is based on the standard Metropolis algorithm [65] and one set of these trials is termed an "MC step".

The phase boundaries are obtained by scanning the chemical potential difference, $\Delta\mu$ versus composition. A plot of such a curve is obtained at every desired temperature and any discontinuity in the latter is interpreted as a phase transition (see [66] and references therein for more details). In order to identify the solubility limit at a given temperature, the average composition of the last three points (which show statistical scatter) is taken before the phase transition occurs, the maximum spread in the latter serving as error bar. By definition the semi-grand canonical ensemble works in a single phase region. Therefore small simulation boxes can be used without loss in accuracy. For our simulations we used boxes containing as little as 1024 atoms and $1.0E+5$ MC steps proved enough to reach full convergence of enthalpy and composition.

The phase boundaries from MMC simulations in grand canonical ensemble are obtained by scanning the temperature (50 K temperature grid) for different compositions (0.25-2% Ni and 0-10% Cr). In this way the phase boundary is determined as the limit below which precipitation is observed and above which solubility is observed. To determine precipitation the solute cluster size distribution averaged over the last five million MC steps is visualized. A monotonous decrease of the cluster size distribution indicates full solubility as none of the cluster nuclei can reach critical size for precipitation. A multi-modal cluster size distribution indicates precipitation as it indicates stable cluster growth of at least one solute cluster. The cluster size distribution function at a given MC step was obtained through a cluster analysis with a second nearest neighbor cut-off criterion.

The disadvantage of simulating precipitation by MMC simulations in grand canonical ensemble is that interface effects can influence the simulation results. Therefore larger simulation boxes are necessary, which makes convergence of the enthalpy slow. On the other hand, the advantage is that these simulations are simple and provide precise information on the precipitate morphology and composition.

For the defect free alloys, boxes of size $5.2 \times 5.2 \times 5.2 \text{ nm}^3$ containing 11,664 atoms were used. For the alloys containing defects (dislocation loops) with Burgers vector $\mathbf{b} = \frac{1}{2} [111]$ the principal axes of the box were oriented along the $[\bar{1}10]$, $[\bar{1}\bar{1}2]$ and $[111]$ directions while for the $\mathbf{b} = [100]$ the principal axes were oriented along the $[100]$, $[010]$ and $[001]$ directions. For the simulation of interstitial $\frac{1}{2}\langle 111 \rangle$ dislocation loops (circular with diameters 2, 3 and 6 nm) and $\langle 100 \rangle$ loops (square-shaped with a side of 3 and 6 nm), cubic boxes of about $5.2 \times 4.2 \times 3.6 \text{ nm}^3$; $10.1 \times 7.0 \times 6.9 \text{ nm}^3$; $12.6 \times 11.2 \times 10.5 \text{ nm}^3$ and $8.6 \times 7.2 \times 7.2 \text{ nm}^3$; $8.3 \times 11.7 \times 11.7 \text{ nm}^3$ were used, respectively. They contain 6,804; 41,820; 127,296 and 37,500; 100,860 atoms, respectively. Five million MC steps were employed for each of these configurations to obtain the average distribution of solute atoms at thermodynamic equilibrium.

For a faster convergence of the MMC simulations, each box – containing the prescribed defect and alloy – was initially thermalized to the required temperature by means of molecular dynamics (MD). This procedure allows the total amount of MC steps before convergence to be reduced by about a factor two. After the MMC simulations, the resulting boxes were relaxed again using a conjugated gradient method. By application of atomic energy and coordination number filters the atoms belonging to the defect were visualized.

3 Results and Discussion

3.1 Basic Properties

To guarantee a physical shape of both FeNi and NiCr cross potentials, they were fitted with low priority to Rose's equation of state [56] for the experimentally observed L_{12} FeNi₃ and Ni₂Cr intermetallic phases, respectively. For completeness, a comparison between experimental/DFT data and data from the potential of the basic properties of both intermetallics is given in Tab. 1. For the L_{12} FeNi₃ intermetallic, agreement with the reference data is good, except for the formation energy. In contrast, agreement with the reference data for the Ni₂Cr intermetallic is poor. The latter is not unexpected: in contrast with the cubic structure of L_{12} FeNi₃, the Ni₂Cr intermetallic has an orthorhombic crystallographic structure that is too complicated to capture within a simple EAM frame work. We note that as reference data for the elastic constants of the Ni₂Cr intermetallic a range is given, which depends on the specific relaxation and loading conditions (see [59] for all details).

Tab. 1 – Comparison between experimental/DFT data and the potential for the elastic constants, lattice parameters and formation energy of the L_{12} FeNi₃ and Ni₂Cr intermetallics.

Property	L_{12} FeNi ₃		Ni ₂ Cr	
	Reference data	Potential	Reference data	Potential
a (Å)	3.55 ^a 3.56 ^b	3.55	3.55 ^d	2.87
b (Å)	3.55 ^a 3.56 ^b	3.55	2.46 ^d	2.87
c (Å)	3.55 ^a 3.56 ^b	3.55	7.36 ^d	7.88
E_f (eV)	-0.089 ^a	0.021	-0.078 ^d -0.043 ^e	0.449
B (GPa)	173 ^c	174		
C_{11} (GPa)	230 ^c	228	302-230 ^d	218
C_{22} (GPa)			333-264 ^d	217
C_{33} (GPa)			348-281 ^d	248
C_{12} (GPa)	144 ^c	147	110-79 ^d	185
C_{13} (GPa)			104-73 ^d	151
C_{23} (GPa)			77-49 ^d	151
C_{44} (GPa)	119 ^c	120	72 ^d	112
C_{55} (GPa)			189 ^d	112
C_{66} (GPa)			176 ^d	147

^a DFT – Ref. [31]

^b Experiment – Ref. [57]

^c Experiment – Ref. [58]

^d DFT – Ref. [59]

^e Experiment – Ref. [60]

In Fig. 1 a comparison of the binding energy of solute-solute and solute-vacancy pairs calculated by both DFT and the potential is presented. Although only the binding energy for Ni-vacancy, Ni-Ni and Cr-Ni pairs were fitted in this work, for completeness all pairs are given. The DFT data is taken from [61], while for the potential the binding energy for vacancy-vacancy pairs is taken from [54] and for Cr-Cr and Cr-vacancy from [35].

We observe that the vacancy-vacancy interaction is well reproduced by the Fe potential [24]. Also the Cr-Cr repulsion and neutral Cr-vacancy interaction are well reproduced by the FeCr potential [35], although the latter with wrong sign.

For our FeNi potential the Ni-Ni interaction is small, similar to the old FeNi potential [34], and in line with DFT [64]. The Ni-vacancy interaction is qualitatively reproduced, i.e., attraction first and second nearest neighbor pairs with strongest attraction at second nearest neighbor is reproduced. Quantitatively the binding is about half the DFT value. For comparison the Ni-vacancy interaction with the old FeNi potential is also included. The latter does not provide any attraction at first nearest neighbor distance. Therefore the present FeNi potential constitutes a significant improvement.

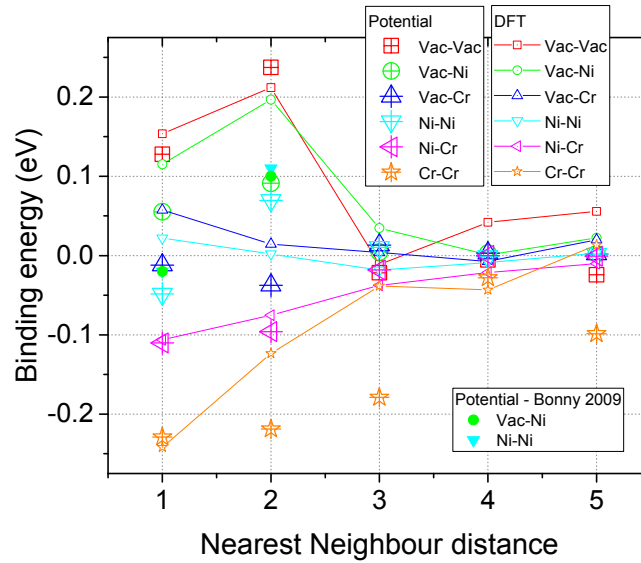


Fig. 1 – Comparison of the binding energy of solute-solute and solute-vacancy pairs calculated by both DFT and the potential.

In **Tab. 2** a comparison of the vacancy-X (X=Fe/Ni/Cr) exchange migration barriers calculated with both DFT and the potential is provided. Although only the vacancy-Ni exchange was fitted in the present work, the other barriers are included for completeness. The values for Fe and Cr are taken from [24] and [35], respectively. Both Ni and Cr migration barriers are in excellent agreement with the most recent DFT data [63, 67]. The vacancy migration barrier in bcc Fe, on the other hand, was fitted to older DFT data [68]. Thus, taking into account the non-negligible spread between different DFT data sets, overall agreement between the potential and DFT is satisfactory.

Tab. 2 – Comparison of the vacancy-X (X=Fe/Ni/Cr) exchange migration barriers calculated with both DFT and the potential.

Barrier	DFT (eV)	Potential (eV)
$E_m(\text{Fe})$	0.64 ^a 0.70 ^b	0.63
$E_m(\text{Ni})$	0.70 ^a 0.63 ^b	0.65 (0.61 ^c)
$E_m(\text{Cr})$	0.53 ^b 0.57 ^d	0.57

^a USPP data, Ref. [68].

^b PAW data, Ref. [63].

^c Old FeNi potential, Ref. [34].

^d PAW data, Ref. [67].

In **Fig. 2** the binding energy of small (substitutional) defect clusters calculated DFT [64] and the potential is compared. A complete list containing the specific configurations and the corresponding binding energy is provided in **Annex II**. Besides the first and second nearest neighbor pairs, none of the other configurations were included in the fit. Based on the linear fit through the data and by comparison with the first bisectant, we conclude that the potential systematically underestimates the DFT data. Indeed, most data points fall below the first bisectant, the slope of the linear fit is smaller than one and the constant term in the linear fit is less than zero. On the other hand, there is a strong correlation between DFT and the potential, i.e., the correlation factor of the data set is $R^2=0.93$, which is close to one. An in-depth analysis of the specific configurations (see **Annex II**) suggests that the bias towards lower binding energy is mainly due to the slightly repulsive interaction between Cr-vacancy pairs and the underestimation of the attraction between Ni-vacancy pairs. Thus, for small (substitutional) defect clusters the potential can reproduce the DFT logic, but is biased to a lower binding energy.

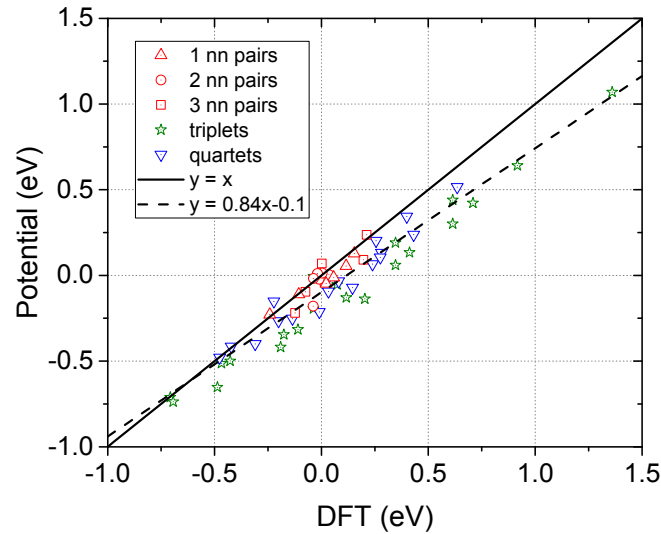
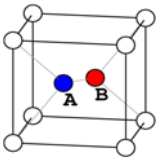
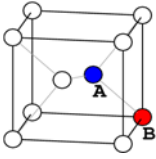


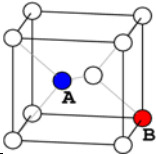
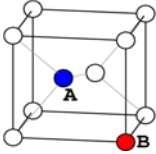
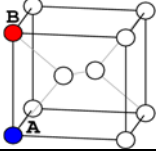
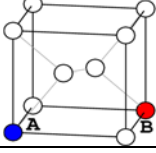
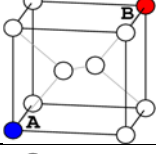
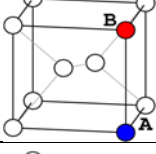
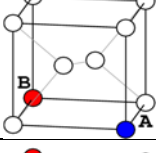
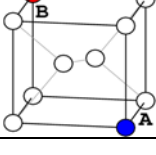
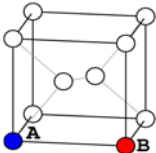
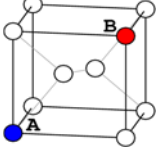
Fig. 2 – Comparison of the total binding energy of CrNiVacancy clusters calculated using DFT and the potential.

In **Tab. 3** the binding energy of several interstitial configurations computed with both DFT [64] and the potential are compared. The configurations that were included in the fit (including the ones fitted for the FeCr potential) are indicated by the symbol *. With respect to solutes in interstitial positions, we note that DFT predicts only the mixed FeCr and NiCr dumbbells to be stable. These features are well reproduced by the potential, although we note that the short distance part of the Ni-Ni pair potential needed to be modified to reproduce the NiNi dumbbell repulsion (see **Annex I**). Without this modification also the NiNi dumbbell is stable.

The most stable interstitial configurations predicted by DFT are the mixed FeCr dumbbell with a Ni atom in compression. This property that was not included in the fit is reasonably well reproduced by the potential, both qualitatively and quantitatively. For the other less- and unstable configurations agreement between DFT and the potential is poor, especially the configurations involving two Cr atoms.

Tab. 3 – Comparison of the binding energy of several interstitial configurations calculated using DFT and the potential. Values included in the fit are marked by *. The most stable configurations are printed in bold. The values for the unmodified Ni-Ni pair potential are given in parentheses.

Configuration	AB	DFT [64]	Potential
	FeNi*	-0.16	-0.16
	FeCr*	0.08	0.08
	NiNi*	-0.13	-0.13 (0.19)
	NiCr*	0.16	0.16
	CrCr	-0.43	-0.22
	FeNi	0.05	0.02
	FeCr	0.05	0.02
	NiNi	-0.05	-0.04 (0.10)
	NiCr	-0.22	-0.02
	CrNi	0.17	0.21
	CrCr	-0.21	-0.17
NiNi	-0.14	-0.18	
NiCr	0.03	-0.18	

	CrNi	0.19	0.09
	CrCr	0.15	-0.18
	FeNi	0.02	-0.07
	FeCr	-0.07	0.09
	NiNi	-0.16	-0.27
	NiCr	-0.28	-0.19
	CrNi	0.06	-0.10
	CrCr	-0.02	-0.04
	NiNi	0.11	0.02
	NiCr	0.08	-0.04
	CrCr	0.12	-0.31
	NiNi	0.10	0.03
	NiCr	0.08	0.04
	CrCr	0.15	-0.10
	NiNi	0.11	0.04
	NiCr	0.08	0.04
	CrCr	0.12	-0.02
	NiNi	0.02	-0.11
	NiCr	-0.07	-0.09
	CrCr	-0.20	-0.03
	NiNi	0.07	-0.14
	NiCr	-0.03	0.00
	CrCr	-0.12	-0.01
	NiNi	0.00	-0.16
	NiCr	-0.05	0.02
	CrCr	-0.12	0.07
	NiNi	0.09	0.04
	NiCr	-0.03	0.05
	CrNi	0.05	-0.12
	CrCr	-0.04	-0.12
	NiNi	0.05	-0.02
	NiCr	-0.03	0.12
	CrNi	0.05	-0.06
	CrCr	-0.04	-0.05

In Fig. 3a the Ni solubility as computed by Calphad [62] and the new and old FeNi potential [34] is compared. Clearly, the present potential signifies a significant improvement over the old one, although the new one still overestimates the Calphad boundary. This short coming is the result of a compromise between the Ni solubility and the Ni-vacancy interaction in bcc Fe. Given this short-coming, any quantitative result with respect to precipitation on defected and ternary alloys represent a lower bound and are therefore conservative estimates.

For completeness we also include the Cr solubility in Fig. 3b (taken from [66]). Below ~750 K agreement between potential and Calphad [69] are excellent. For more details and a complete discussion regarding the thermodynamics of the FeCr potential we refer to [35, 66].

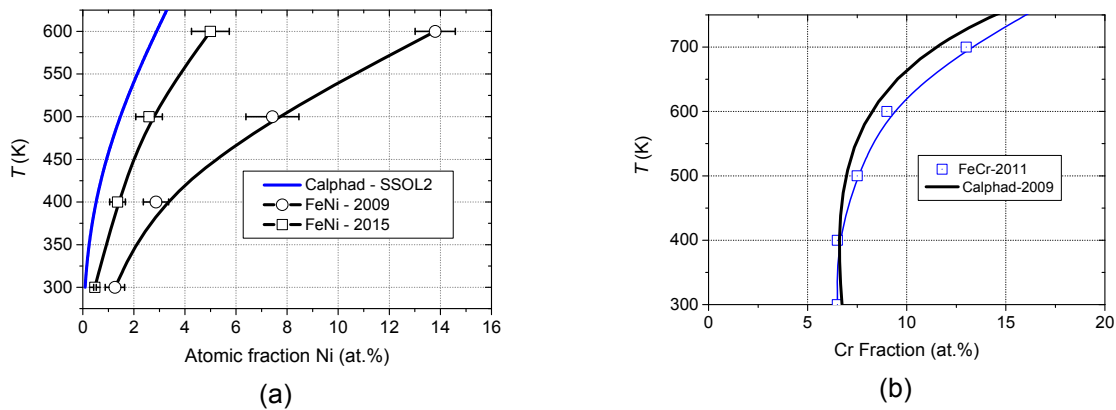


Fig. 3 – Comparison between Calphad calculations and the potentials of the Ni (a) and Cr (b) solubility in bcc Fe.

3.2 Thermal Stability of Nickel Chromium Clusters

3.2.1 Defect Free Alloys

As explained in Section 2.2, from our MMC simulations in grand canonical ensemble precipitation and full solubility are derived from the cluster size distribution. In Fig. 4 a representative example of the cluster size distribution yielding precipitation and full solubility is given. For both cases the integrated distribution size is normalized to unity. In the example for an Fe-1Ni alloy, the bimodal distribution at 450 K indicates precipitation, while the unimodal distribution at 400 K indicates full solubility. As a result, the solubility limit for Fe-1Ni lays at 425 ± 25 K.

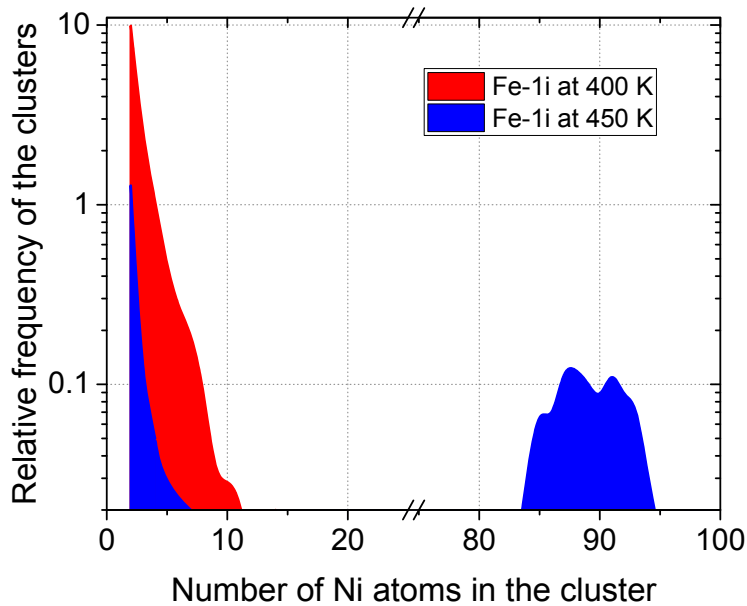


Fig. 4 – Averaged Ni cluster size distribution.

Prior to discussing the results in terms of Ni and Cr solubility, we mention that our cluster analysis revealed that Ni and Cr do not mix in precipitates. They both precipitate as separate fractions. This observation is in line with the repulsion of NiCr pairs shown in Fig. 1 and repulsion of mixed NiCr clusters (see Table B1 in Annex II), observed by both DFT and the potential.

In Fig. 5 the solubility limit of Ni and Cr resulting from the grand canonical MMC simulations for the investigated alloys is presented. To verify consistency of this method, the Ni and Cr solubility limit obtained from semi-grand canonical MMC simulations (see Fig. 3) is superposed in the figure. Clearly, the curves (point for Cr) resulting from both methods fall within each other's error bar.

For the ternary alloys, we observe that the addition of Ni to Fe-10Cr shows no influence on the clustering of Cr, within the error bar of the calculations. Indeed, the curve remains horizontal within the error bar. For Ni clusters, only a significant effect for 2% Ni is observed, i.e., the Ni solubility limit is raised by ~100 K.

Thus, in defect free alloys there is a limited synergetic effect on the Ni solubility, which manifests at high Ni content; and the presence of Ni has no influence on the Cr solubility.

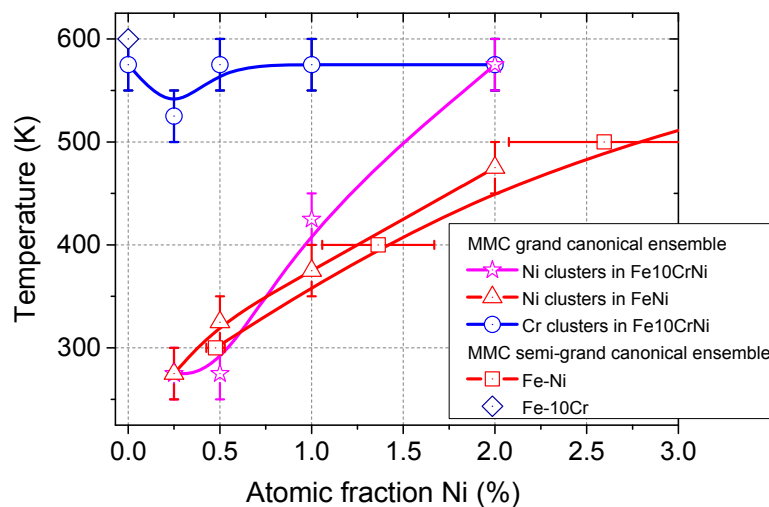


Fig. 5 – Phase boundaries indicating the formation of Cr and Ni clusters in Fe10CrNi alloys and their binaries.

3.2.2 Dislocation Loops

We mention that all results presented in this section were calculated using the unmodified Ni-Ni pair potential. We start this section by comparing the solubility limit of Ni and Cr in the presence of defects with the defect free solubility limit. With respect to Cr, the presence of dislocation loops has a small effect on the solubility limit. As shown in Fig. 6, the solubility limit of Cr increases by at most 100 K, depending on the Ni content and dislocation loop type. Loops of $\frac{1}{2}\langle 111 \rangle$ type increase Cr solubility the most.

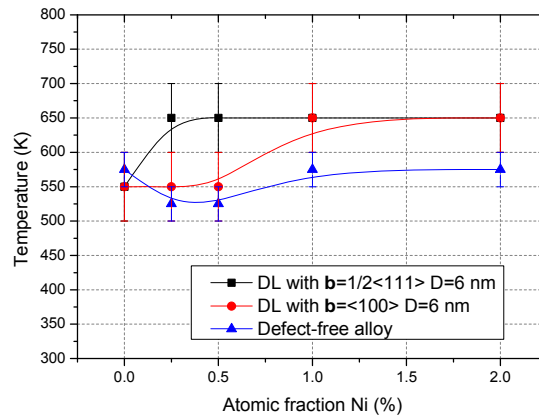


Fig. 6 – Comparison of the Cr solubility in Fe-10Cr-Ni alloys and their binaries between defect free crystals and crystals containing dislocation loops.

In Fig. 7 the effect of dislocation loops on the Ni solubility is presented. In binary FeNi alloys (see Fig. 7a) only loops with $b=\langle 100 \rangle$ increase the solubility limit by about 200 K and the effect does not depend on concentration of Ni. In Fe-10Cr-Ni (see Fig. 7b) both dislocation loops with $b=\frac{1}{2}\langle 111 \rangle$ and $b=\langle 100 \rangle$ contribute to the increase of Ni solubility, starting from 1% and 0.5% Ni, respectively. In these cases the Ni solubility raises by 100-150 K compared to binary FeNi alloys. Thus, in addition to the loops, also Cr plays a stabilizing role for the formation of Ni clusters.

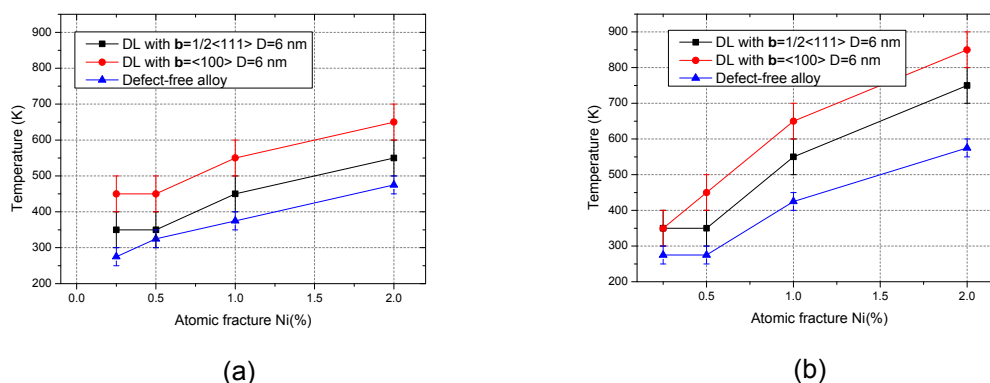


Fig. 7 – Comparison of the Ni solubility in a) FeNi and b) Fe-10Cr-Ni alloys between defect free crystals and crystals containing dislocation loops.

Given the change in both Cr and Ni solubility due to the presence of dislocation loops, we analyze the segregation of both Cr and Ni at both loop types. The segregation of Cr in Fe10Cr was already studied in [15] using the potential developed by Olsson et al [33]. For comparison, the Cr enrichment of loops for both potentials is summarized in Fig. 8, where Fig. 8a is taken from [15]. In [15] strong segregation (35-40%) of Cr at both types of dislocation loops (with $b=\frac{1}{2}\langle 111 \rangle$ and $b=\langle 100 \rangle$) at temperatures 300 K and 600 K was reported,

and moderate segregation (25%) at 900 K. Segregation at $\frac{1}{2}\langle 111 \rangle$ loops is stronger than at $\langle 100 \rangle$, which is consistent with our MMC calculations.

Our results (see Fig. 8b) show pronounceable segregation (>15%) at $T \leq 700$ K for $\frac{1}{2}\langle 111 \rangle$ loops and $T \leq 400$ K for $\langle 100 \rangle$ loops. There is a size effect for $\frac{1}{2}\langle 111 \rangle$ loops only: at 300 K more segregation is observed at the larger loop.

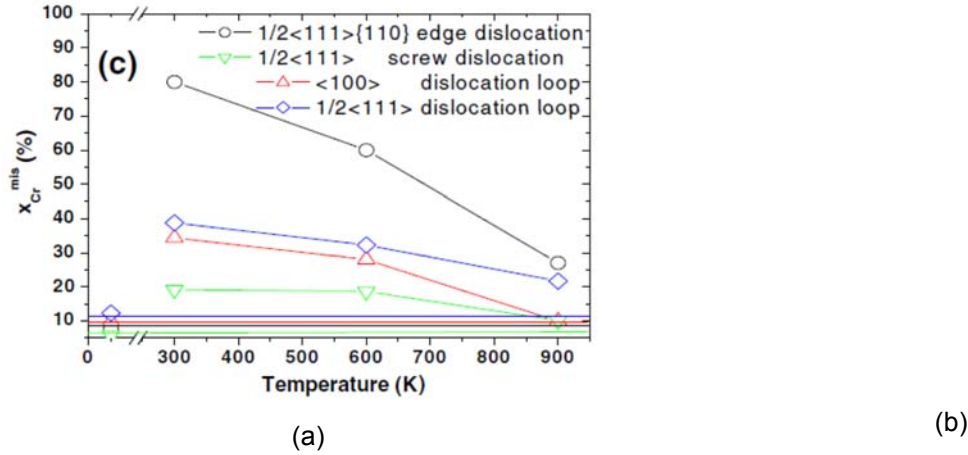


Fig. 8 – Cr enrichment at dislocation loops in Fe-10Cr studied with a) the potential by [33] and b) our potential. Panel (a) of the figure is taken from [15].

In Fig. 9 the results for Cr segregation on $\frac{1}{2}\langle 111 \rangle$ and $\langle 100 \rangle$ loops of size 6 nm are presented. The figure shows that segregation of Cr is pronounceable (above 15%) at $T \leq 600$ K for Fe-10Cr-0.25Ni and Fe-10Cr-0.50Ni. At 1.0% Ni we observe segregation (up to 16%) for loops with $b=\frac{1}{2}\langle 111 \rangle$ and depletion of the loops with $b=\langle 100 \rangle$. At 2% Ni the loop is depleted further down to 5% of Cr. Thus, the increase of Ni generally decreases loop enrichment with Cr. A size effect is observed only for loops with $b=\frac{1}{2}\langle 111 \rangle$. A larger loop leads to more segregation or stronger depletion for the cases of segregation and depletion, respectively. As a result we also state that the segregation or depletion on $\frac{1}{2}\langle 111 \rangle$ loops is stronger than on $\langle 100 \rangle$ loops.

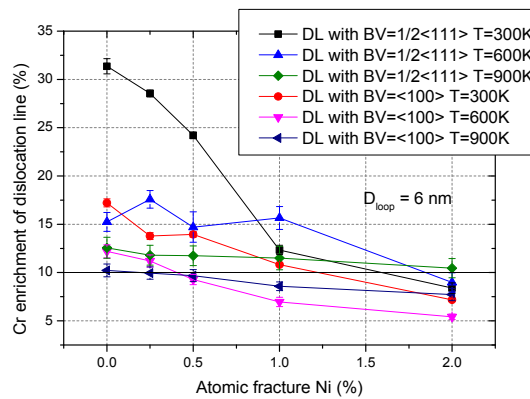


Fig. 9 – Cr segregation of Cr at dislocation loops in Fe-10Cr-Ni alloys.

In Fig. 10 the enrichment of dislocation loops in the FeNi and Fe-10Cr-Ni alloys is presented. In FeNi significant segregation (above 5%) is observed at $T \leq 500$ K for Fe-0.25Ni, $T \leq 600$ K for Fe-0.50Ni, $T \leq 800$ K for Fe-1.00Ni and up to 1000 K for Fe-2.00Ni. In Fe-10Cr-Ni significant segregation (above 5%) is observed at $T \leq 500$ K for Fe-0.25Ni, $T \leq 700$ K for Fe-10Cr-0.50Ni, $T \leq 900$ K for Fe-10Cr-1.00Ni and up to 1000 K for Fe-10Cr-2.00Ni. A size effect is observed only for $\frac{1}{2}\langle 111 \rangle$ loop in FeNi where larger loops lead to more enrichment. In FeNi alloys the segregation of Ni is stronger than in Fe-10Cr-Ni up to 1% for $\langle 100 \rangle$ loops and for all studied concentrations for $\frac{1}{2}\langle 111 \rangle$ loops. In general, the segregation of Ni is very strong, reaching values of 10-30% at 300 K, 4-25% at 600 K, 3-10% at 900 K depending on initial concentration of Ni.

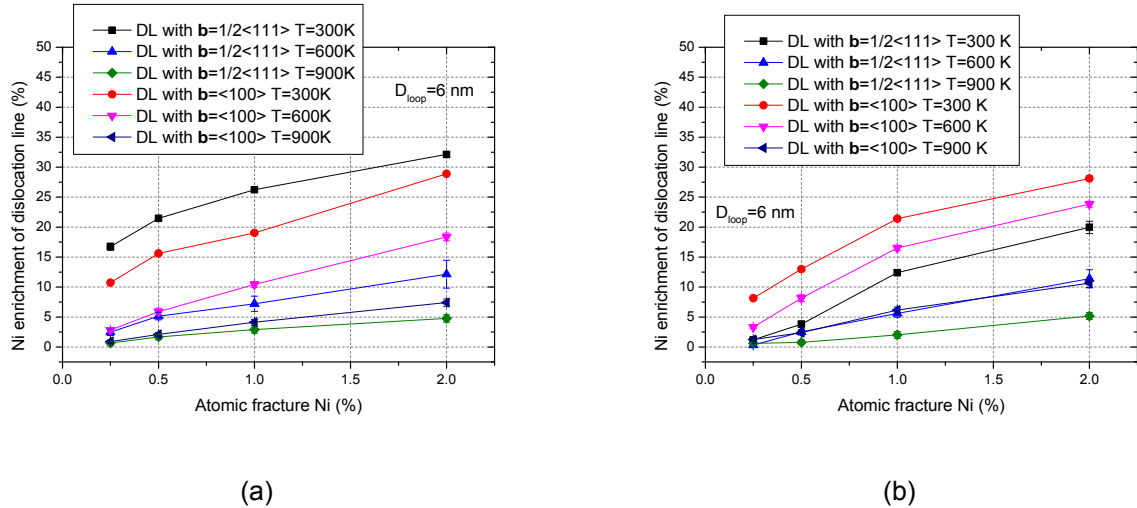


Fig. 10 – Segregation of Ni at dislocation loops in a) FeNi alloys and b) Fe-10Cr-Ni alloys.

To investigate a possible synergy between Ni and Cr, we have compared the total segregation of Ni and Cr in the ternary with the sum of the Cr and Ni segregation in the binaries. The results are presented in Fig. 11. No visible synergy is found except for the case of dislocation loops with $b=1/2\langle 111 \rangle$ at 300 K where the total segregation in Fe-10Cr-Ni is much lower than the cumulative segregation in Fe-10Cr and relevant FeNi alloys. This effect is related to a significantly stronger segregation of Cr at such loops in Fe-10Cr alloys and much lower segregation in Fe-10Cr-Ni alloys compared to FeNi.

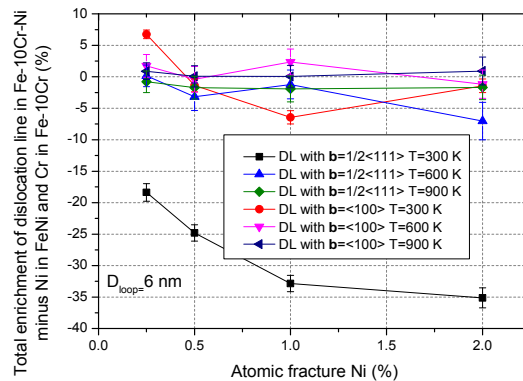


Fig. 11 – Total segregation at dislocation loops in FeNiCr alloys minus the segregation of Ni in FeNi and of Cr in Fe-10Cr.

4 Conclusions

We have developed a ternary potential for the ferritic FeNiCr system and applied it to study the formation of NiCr clusters near dislocation loops by means of MMC simulations. The potential was fitted to point defect properties and the Ni solubility limit in bcc Fe.

The potential has shown to reproduce the most stable interstitial configurations predicted by DFT. In addition, the potential can reproduce DFT logic with respect to the binding energy of small substitutional defect clusters.

In defect free alloys the MMC simulations have shown that the presence of Cr slightly increases the Ni solubility, while the presence of Ni does not affect the Cr solubility.

From our MMC simulations we found that the presence of dislocation loops increases the Cr solubility limit by about 100 K for low concentrations of Ni, i.e., in Fe-10Cr-0.25Ni and Fe-10Cr-0.50Ni alloys. In Fe-10Cr-Ni alloys both $1/2\langle 111 \rangle$ and $\langle 100 \rangle$ loops contribute to the increase of Ni solubility, starting from concentrations of Ni equal to 1% and 0.5%, respectively. Thus, Cr plays a stabilizing role for the Ni clusters

while the addition of Ni decreases the segregation of Cr, leading to depletion of Cr above 1% of Ni. In FeNi alloys the segregation of Ni at dislocation loops is stronger than in Fe-10Cr-Ni up to 1% for $\langle 100 \rangle$ loops and for all concentrations of Ni studied for $\frac{1}{2}\langle 111 \rangle$ loops.

No synergetic effects were found for Ni and Cr with respect to segregation, except for the case of $\frac{1}{2}\langle 111 \rangle$ dislocation loops at 300 K where the total segregation in Fe-10Cr-Ni is much lower than the cumulative segregation in Fe-10Cr and relevant FeNi alloys.

5 Annex I: Parameterization of the Potential

The atomic interactions are described using the two-band model (2BM) [33]. The total energy is given as in the EAM [21] with an extra embedding term, F^s ,

$$E = \frac{1}{2} \sum_{i,j=1}^N V_{t_i t_j}(r_{ij}) + \sum_{i=1}^N F_{t_i}^d(\rho_i^d) + \sum_{i=1}^N F_{t_i}^s(\rho_i^s). \quad (\text{A1})$$

Here N represents the total number of atoms in the system, r_{ij} is the distance between atoms i and j , and t_i denotes chemical species (Fe, Ni and Cr in our case). The additional embedding term on the right-hand side is assumed to stem from the s-band electrons, while the standard embedding, F^d , is thought of as resulting from the d-band electrons [33]. The electron densities, ρ^d and ρ^s , for the d- and s-band, respectively, are calculated as,

$$\rho_i^\lambda = \sum_{j=1}^N \varphi_{t_i t_j}^\lambda(r_{ij}). \quad (\text{A2})$$

Here, φ^d and φ^s are the d- and s-density functions, respectively, which comply with the relations,

$$\begin{cases} \varphi_{XY}^d = \varphi_Y^d \\ \varphi_{XX}^s = 0 \\ \varphi_{XY}^s = \varphi_{YX}^s \end{cases}. \quad (\text{A3})$$

In this way, the s-embedding terms are only relevant for the alloy and do not contribute to the pure elements' energy, which keeps the standard EAM expression.

In this work we chose $F_{\text{Ni}}^s = 0$ and $\varphi_{\text{FeNi}}^s = \varphi_{\text{NiCr}}^s = 0$. Thus, given the binary 2BM FeCr potential by Bonny et al [35] and the EAM Ni potential by Mishin et al [25], only V_{FeNi} and V_{NiCr} need to be determined. The pair potentials are parameterized as,

$$V(r) = \sum_{k=1}^{N_p} [a_k (r_k - r)^3 \theta(r_k - r)], \quad (\text{A4})$$

with a_k the spline coefficients, r_k the knots and θ is the Heaviside function. The optimized parameters are summarized in Tab. A1.

To obtain repulsion of the NiNi dumbbell in bcc Fe (see Tab. 3 in Section 3.1), the spline function (see equation A4) as parameterized in Tab. A1 has to be added to the one published in [25]. We emphasize that this short range modification does not change any of the results reported in [25].

Tab. A1 – The optimized parameter set for the present potential.

FeNi			NiCr		
k	r_k	a_k	k	r_k	a_k
1	2.300000E+00	4.223995E+01	1	2.300000E+00	3.200000E+00
2	2.941667E+00	2.497327E+00	2	2.000000E+00	4.262123E+01
3	3.583333E+00	-5.753098E-01	3	2.833333E+00	1.520775E+00
4	4.225000E+00	2.025327E-01	4	3.666667E+00	-3.043511E-02
5	4.866667E+00	-5.694582E-02	5	4.500000E+00	-2.511316E-02

NiNi		
1	2.3	70

6 Annex II: Binding Energy of Small Defect Clusters

In [Tab. B1](#) a comparison between DFT and potential for the binding energy of small substitutional defect clusters is presented. The configurations correspond to the ones used in [Fig. 2](#) in [Section 3.1](#). The topology of the specific configurations is provided in [Fig. B1](#). The data in the table shows that vacancy clusters are the most stable and that the addition of Ni or Cr reduces their stability.

Tab. B1 – Comparison between DFT and potential for the binding energy of small substitutional defect clusters. The topology of the specific configurations is provided in [Fig. B1](#).

Pairs {1,2} (1nn)	DFT (eV)	Pot. (eV)	Pairs {1,3} (2nn)	DFT (eV)	Pot. (eV)
V V	0.15	0.13	V V	0.21	0.24
V Ni	0.12	0.06	V Ni	0.20	0.09
V Cr	0.06	-0.01	V Cr	0.01	-0.04
Ni Ni	0.02	-0.05	Ni Ni	0.00	0.07
Ni Cr	-0.11	-0.11	Ni Cr	-0.08	-0.10
Cr Cr	-0.24	-0.23	Cr Cr	-0.12	-0.22
Pairs {1,4} (3nn)	DFT (eV)	Pot. (eV)	Pairs {1,5} (4nn)	DFT (eV)	Pot. (eV)
V V	-0.01	-0.02	V V	0.04	-0.01
V Ni	0.03	0.00	V Ni	0.00	0.00
V Cr	0.00	0.01	V Cr	-0.01	0.00
Ni Ni	-0.02	0.01	Ni Ni	-0.01	0.00
Ni Cr	-0.04	-0.02	Ni Cr	-0.02	0.00
Cr Cr	-0.04	-0.18	Cr Cr	-0.04	-0.03
Pairs {1,6} (5nn)	DFT (eV)	Pot. (eV)			
V V	0.06	-0.02			
V Ni	0.02	0.00			
V Cr	0.02	0.00			
Ni Ni	0.00	0.00			
Ni Cr	-0.01	0.00			
Cr Cr	0.01	-0.10			
Triplets {2,3,4}	DFT (eV)	Pot. (eV)	Quartets {2,5,3,4}	DFT (eV)	Pot. (eV)
V V V	0.64	0.52	Cr Cr Cr Cr	-0.71	-0.71
V V Ni	0.43	0.24	Ni Ni Ni Ni	0.07	-0.05
V V Cr	0.24	0.07	V V V V	1.36	1.07
V Ni Ni	0.28	0.13	Cr Cr Cr Ni	-0.69	-0.74
V Ni Cr	0.15	-0.07	Cr Cr Cr V	-0.43	-0.50
V Cr Cr	-0.01	-0.21	Ni Ni Ni Cr	-0.18	-0.35
Ni V V	0.40	0.34	Ni Ni Ni V	0.41	0.13
Ni V Ni	0.28	0.11	V V V Cr	0.71	0.42
Ni V Cr	0.03	-0.09	V V V Ni	0.92	0.64
Ni Ni Ni	0.03	-0.02	Cr Cr Ni Ni	-0.47	-0.51
Ni Ni Cr	-0.14	-0.25	Cr Ni Cr Ni	-0.49	-0.65

Ni Cr Cr	-0.31	-0.40	Cr Cr V V	-0.04	-0.01
Cr V V	0.26	0.20	Cr V Cr V	-0.04	-0.19
Cr V Ni	0.08	-0.03	Ni Ni V V	0.61	0.44
Cr V Cr	-0.20	-0.27	Ni V Ni V	0.61	0.30
Cr Ni Ni	-0.22	-0.15	Cr Cr Ni V	-0.11	-0.32
Cr Ni Cr	-0.42	-0.42	Cr Ni Cr V	-0.19	-0.42
Cr Cr Cr	-0.48	-0.48	Ni Ni Cr V	0.12	-0.13
			Ni Cr Ni V	0.20	-0.14
			V V Cr Ni	0.35	0.19
			V Cr V Ni	0.35	0.06

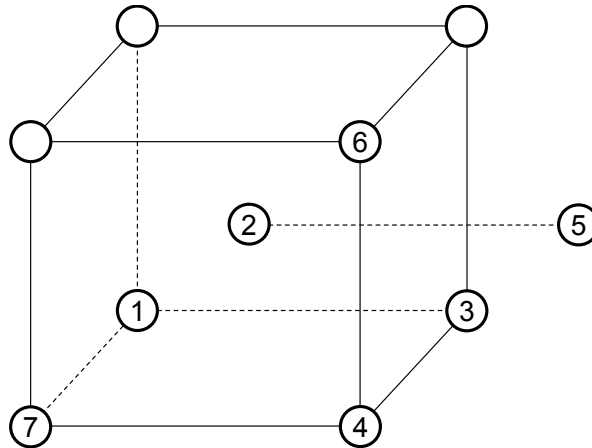


Fig. B1 – Atomic positions to indicate the topology of clusters.

References

- [1] L.K. Mansur, A.F. Rowcliffe, R.K. Nanstad, S.J. Zinkle, W.R. Corwin, R.E. Stoller, *J. Nucl. Mater.* 329-333 (2004) 166.
- [2] C. Fazio, A. Alamo, A. Almazouzi, S. De Grandis, D. Gomez-Briceno, J. Henry, L. Malerba, M. Rieth, *J. Nucl. Mater.* 392 (2009) 216.
- [3] C. Fazio, D.G. Briceno, M. Rieth, A. Gessi, J. Henry, L. Malerba, *Nucl. Eng. Des.* 241 (2011) 3514.
- [4] Y. Dai, J. Henry, T. Auger, J.-B. Vogt, A. Almazouzi, H. Glasbrenner, F. Groeschel, *J. Nucl. Mater.* 356 (2006) 308.
- [5] M. Matijasevic and A. Almazouzi, *J. Nucl. Mater.* 377 (2008) 147.
- [6] F. Bergner, A. Ulbricht, C. Heintze, *Scr. Mater.* 61 (2009) 1060.
- [7] V. Kuksenko, C. Pareige, C. Genevois, F. Cuvilly, M. Roussel and P. Pareige, *J. Nucl. Mater.* 415 (2011) 61.
- [8] F. Bley, *Acta Metall. Mater.* 40 (1992) 1505.
- [9] S. Novy, P. Pareige, and C. Pareige, *J. Nucl. Mater.* 384 (2009) 96.
- [10] D.A. Terentyev, G. Bonny and L. Malerba, *Acta Mater.* 56 (2008) 3229.
- [11] G. Bonny, D. Terentyev, L. Malerba and D. Van Neck, *Phys. Rev. B* 79 (2009) 104207.
- [12] D. Terentyev, G. Bonny, C. Domain and R.C. Pasianot, *Phys. Rev. B* 81 (2010) 214106.
- [13] C. Pareige, M. Roussel, S. Novy, V. Kuksenko, P. Olsson, C. Domain and P. Pareige, *Acta Mater.* 59 (2011) 2404.
- [14] F. Bergner, C. Pareige, V. Kuksenko, L. Malerba, P. Pareige, A. Ulbricht and A. Wagner, *J. Nucl. Mater.* 442 (2013) 463.
- [15] E.E. Zhurkin, D. Terentyev, M. Hou, L. Malerba and G. Bonny, *J. Nucl. Mater.* 417 (2011) 1082.
- [16] D. Terentyev and A. Bakaev, *J. Phys. Condens. Matter* 25 (2013) 265702.
- [17] D. Terentyev, F. Bergner and Y. Osetsky, *Acta Mater.* 61 (2013) 1444.
- [18] V. Kuksenko, C. Pareige and P. Pareige, *J. Nucl. Mater.* 425 (2012) 125.
- [19] V. Kuksenko, C. Pareige and P. Pareige, *J. Nucl. Mater.* 432 (2013) 160.
- [20] C. Pareige, V. Kuksenko and P. Pareige, *J. Nucl. Mater.* 456 (2015) 471.
- [21] M. S. Daw and M.I. Baskes, *Phys. Rev. B* 29 (1984) 6443.

- [22] R.A. Johnson, Phys. Rev. B 37 (1988) 3924.
- [23] R.A. Johnson and D.J. Oh, J. Mater. Res. 4 (1989) 1195.
- [24] M.I. Mendeleev, S. Han, D.J. Srolovitz, G.J. Ackland, D.Y. Sun and M. Asta, Philos. Mag. 83 (2003) 3977.
- [25] Y. Mishin, Acta Mater. 52 (2004) 1451.
- [26] R.W. Smith and G.S. Was, Phys. Rev. B 40 (1989) 10322.
- [27] M. Grujicic and X.W. Zhou, CALPHAD 17 (1993) 383.
- [28] M. Grujicic and P. Dang, Mater. Sci. Eng. A 201 (1995) 194.
- [29] M. Grujicic, S. Lai and P. Gumbsch, Mater. Sci. Eng. A 231 (1997) 151.
- [30] R. Meyer and P. Entel, Phys. Rev. B 57 (1998) 5140.
- [31] Y. Mishin, M.J. Mehl and D.A. Papaconstantopoulos, Acta Mater. 53 (2005) 4029.
- [32] A. Caro, D.A. Crowson and M. Caro, Phys. Rev. Lett. 95 (2005) 75702.
- [33] P. Olsson, J. Wallenius, C. Domain, K. Nordlund and L. Malerba, Phys. Rev. B 72 (2005) 214119.
- [34] G. Bonny, R.C. Pasianot and L. Malerba, Modelling Simul. Mater. Sci. Eng. 17 (2009) 025010.
- [35] G. Bonny, R.C. Pasianot, D. Terentyev and L. Malerba, Philos. Mag. 91 (2011) 1724.
- [36] G. Bonny, D. Terentyev, R.C. Pasianot, S. Poncé and A. Bakaev, Modelling Simul. Mater. Sci. Eng. 19 (2011) 085008.
- [37] E. del Rio, J. M. Sampedro, H. Dogo, M.J. Caturla, M. Caro, A. Caro, J.M. Perlado, J. Nucl. Mater. 408 (2011) 18.
- [38] G. Bonny, N. Castin and D. Terentyev, Modelling Simul. Mater. Sci. Eng. 21 (2013) 085004.
- [39] S.M. Eich, D. Beinke and G. Schmitz, Comp. Mater. Sci. 104 (2015) 185.
- [40] P. Olsson, I.A. Abrikosov, L. Vitos, J. Wallenius, J. Nucl. Mater. 321 (2003) 84.
- [41] A.A. Mirzoev, M.M. Yalalov, D.A. Mirzaev, Phys. Met. & Metall. 97 (2004) 336.
- [42] T.P.C. Klaver, R. Drautz and M.W. Finnis, Phys. Rev. B 74 (2006) 094435.
- [43] P. Olsson, I.A. Abrikosov and J. Wallenius, Phys. Rev. B 73 (2006) 104416.
- [44] D. Nguyen-Mahn, M. Yu. Lavrentiev and S.L. Dudarev, J. Computer-Aided Mater. Des. 14 (2007) 159.
- [45] P. Olsson, C. Domain and J. Wallenius, Phys. Rev. B 75 (2007) 014110.
- [46] P. Erhart, B. Sadigh, A. Caro, Appl. Phys. Lett. 92 (2008) 141904.
- [47] D. Terentyev, G. Bonny, C. Domain and R.C. Pasianot, Phys. Rev. B 81 (2010) 214106.
- [48] T.P.C. Klaver, G. Bonny, P. Olsson and D. Terentyev, Modelling Simul. Mater. Sci. Eng. 18 (2010) 075004.
- [49] D. Terentyev, G. Bonny, N. Castin, C. Domain, L. Malerba, P. Olsson, V. Molodtsov, R.C. Pasianot, J. Nucl. Mater. 409 (2011) 167.
- [50] G. Bonny, D. Terentyev, L. Malerba, J. Nucl. Mater. 416 (2011) 70.
- [51] E.E. Zhurkin, D. Terentyev, M. Hou, L. Malerba, G. Bonny, J. Nucl. Mater. 417 (2011) 1082.
- [52] N. Castin, G. Bonny, D. Terentyev, M.Yu. Lavrentiev, D. Nguyen-Manh, J. Nucl. Mater. 417 (2011) 1086.
- [53] G. Bonny, D. Terentyev, A. Bakaev, E.E. Zhurkin, M. Hou, D. Van Neck, L. Malerba, J. Nucl. Mater. 442 (2013) 282.
- [54] L. Malerba, M.C. Marinica, N. Anento, C. Björkas, H. Nguyen, C. Domain, et al., J. Nucl. Mater. 406 (2010) 19.
- [55] C. Domain, G. Monnet, Phys. Rev. Lett. 95 (2005) 215506.
- [58] G. Simmons and H. Wang, "Single crystal elastic constants and calculated aggregate properties", Cambridge (MA), MIT Press, 1977.
- [56] J.H. Rose, J.R. Smith, F. Guinea and J. Ferrante, Phys. Rev. B 29 (1984) 2963.
- [57] A. Lutts and P.M. Gielen, Phys Status Solidi 41 (1970) K81.
- [59] K.S. Chan, Y.-D. Lee and Y.-M. Pan, Metall. Mater. Trans. A 37A (2006) 523.
- [60] M. Hirabayashi, M. Koiwa, K. Tanaka, T. Tadaki, T. Saburi, S. Nenno and H. Nishiyama, Trans. JIM 10 (1969) 365.
- [61] P. Olsson, T.P.C. Klaver, C. Domain, Phys. Rev. B 81 (2010) 054102.
- [62] B. Sundman, SSOL database, 1993.
- [63] L. Messina, M. Nastar, T. Garnier, C. Domain and P. Olsson, Phys. Rev. B 90 (2014) 104203.
- [64] P. Olsson and C. Domain, DFT calculations within MATISSE.
- [65] M. P. Allen and D. Tildesley, "Computer Simulation of Liquids", Clarendon Press, Oxford, (1987).
- [66] G. Bonny, R.C. Pasianot, E.E. Zhurkin and M. Hou, Comp. Mater. Sci. 50 (2011) 2216.
- [67] D. Nguyen-Manh, M.Y. Lavrentiev and S.L. Dudarev, Comp. Rendus Phys. 9 (2008) 379.
- [68] E. Vincent, C.S. Becquart and C. Domain, J. Nucl. Mater. 351 (2006) 88.
- [69] G. Bonny, D. Terentyev and L. Malerba, J. Phase Eq. Diff. 31 (2010) 439.